Materials Advances

PAPER

Check for updates

Design of Co₁Al₃(OH)ₘ/carbon nitride hybrid nanostructures for enhanced capacitive energy storage in an alkaline electrolyte†

Prajnashree Panda, Ranjit Mishra, [ID] Sonali Panigrahy and Sudip Barman [ID] *

Over the past few years, layered double hydroxide (LDH) nanostructures have attracted the attention of the scientific community owing to their facile synthesis, interesting structure and morphology, and have been promising in the field of energy storage applications. In this work, we have synthesized CoAl LDH over a graphitic carbon nitride (CN$_x$) surface by varying the ratio of Co : Al and among them, the Co₁Al₃(OH)ₘ/CN$_x$ composite was found to have the maximum electrochemical behaviour for supercapacitor application in alkaline electrolytes. Interestingly, it exhibits a 3D nano flower-like structure which provides a high specific capacitance (C_s) value of 138 mA h g^{-1} (1000 F g^{-1}) at 1 A g^{-1} current density and cyclic durability of approximately 84.46% after 4500 cycles at 10 A g^{-1} current density. In addition, we obtained a specific capacitance of 71.5 F g^{-1} at 1 A g^{-1} current density along with long-term cyclic stability for the asymmetric supercapacitor (ASC) Co₁Al₃(OH)ₘ/CN$_x$//AC assembled with Co₁Al₃(OH)ₘ/CN$_x$ and activated carbon (AC) as the positive and negative electrodes respectively. Furthermore, an energy density of 22.35 W h kg^{-1} is obtained at 750.2 W kg^{-1} power density in ASC. The enhanced charge storage property of the aforementioned material can be attributed to the high surface area of the composite and the synergetic interaction between CN$_x$ and CoAl-LDH. Moreover, this facile synthesis method is promising for designing a novel and cost-effective electrode material for supercapacitor applications.

Introduction

The depletion of fossil fuels and the rising environmental concerns have made the development of sustainable and clean energy sources crucial.[1–3] The ever-increasing demand for modern electric vehicles and electronic devices promotes the growth of highly efficient energy storage devices with high energy density as well as high power density. Out of several energy storage devices, supercapacitors have gained enormous attention owing to their long life cycles, high power density and safe operation.[2,4] Compared to conventional secondary batteries, supercapacitors offer promising power efficiencies to meet the demands of practical applications. Based on the energy storage mechanism, general supercapacitors are classified as electrical double-layer capacitors (EDLCs) and pseudocapacitors.[5,6] In fact, EDLCs work through the adsorption of electrolytic ions on the electrode surface and pseudocapacitors work on the basis of the

existence of faradaic redox reactions during the charge–discharge process.[7,8] Examples of EDLCs include carbon-based materials, while pesudocapacitors include metal oxides, hydroxides and sulfides *etc.*[9,10] Therefore designing better supercapacitors relies on developing electrode materials with noticeable capacity values.

In electrochemical applications, layered double hydroxides (LDHs) have appeared as promising materials towards applications like water electrolysis and supercapacitors.[2,11] LDHs are composed of both divalent and trivalent metal cations with a general formula of $[M(II)_{1-x}M(III)_x(OH)_2]^{x+}[A^{n-}]_{x/n}\cdot zH_2O$, where A is an anion. Also, LDHs can intercalate and exchange anions. Since LDHs can provide many electrochemical active sites, they are potential materials that could improve the capacity of modern electrochemical capacitors. However, the low rate of diffusion of mass and electron transfer restricts the high charge–discharge capability of LDHs.[1] Several efforts have been made to design LDH-based supercapacitor electrodes using non-precious metals, and different strategies such as designing a porous morphology, controlling the size of the nanocomposite, amorphization of materials, synthesizing oxygen-deficient materials or defect-rich materials, and tuning the composition of LDH have been adopted for enhanced

School of Chemical Sciences, National Institute of Science Education and Research (NISER), HBNI, Bhubaneswar, Orissa-752050, India. E-mail: sbarman@niser.ac.in; Tel: +91-674-2494183

† Electronic supplementary information (ESI) available. See DOI: 10.1039/d1ma00665g

capacitive behaviour.[12] Previously it has been reported that the molar ratio of trivalent and divalent ions affects the morphology, structure and charge storage capacity of LDHs. Recently, Wu *et al.* used NiAl-LDH as an electrode material for a supercapacitor and investigated the impact of change in the molar feeding ratio of Ni and Al on the capacitive performance of the LDH.[13] The results revealed that the LDH with a Ni/Al ratio of 3 provides the maximum specific capacitance value along with a stable lifecycle. The introduction of aluminium broadened the inter-layer spacing and improved the ion diffusion kinetics of LDH. Recently some other reports have also explored the fact that the change in molar ratio of Co/Ni can change the morphology of the NiCo LDH.[14] Moreover tuning of the metal ion composition in LDHs can be crucial for improving the capacitive behaviour of the material and the electronic behaviour of active electrode materials can be enhanced *via* doping low-cost other metals like Al and Cu *etc.*

In addition, the performance of LDHs can be optimized *via* preparing hybrid composites with two-dimensional carbon-based materials (graphene, carbon nanotube and carbon nitride *etc.*) which can provide better charge transfer, electronic conductivity and high surface area to the composite material arising from the synergistic interactions between the components.[9] Recently nitrogen-doped carbon materials have gained attention for energy storage applications, as the presence of nitrogen provides electron pairs to the carbon materials which results in enhanced electronic conductivity.[15] Recently Tian *et al.* synthesized a hybrid composite of NiAl LDH and nitraime-N doped graphene which showed an enhanced capacitive performance.[16] The presence of N improved the electrostatic interaction between carbon sheets and NiAl LDH and also enhanced the amount of Ni(III) ion in the material. The composite material provided increased electrochemical active sites and better electron transport during the redox reaction at the electrode–electrolyte interface. Also graphitic carbon nitride could specifically enhance the pseudocapacitive property of composites through its high nitrogen content providing surface polarity and better electron donor capacity. Although few reports of CN_x supported LDHs have been published in recent times, there is a need for research on CN_x supported hybrid nanocomposites for supercapacitor application.[17]

In this work, we propose a single step one pot synthesis of $Co_1Al_3(OH)_m/CN_x$ composite for supercapacitor application. The growth and *in situ* nucleation of $Co_1Al_3(OH)_m$ over carbon nitride results in the formation of a 3D nanoflower type structure with a smooth surface. The $Co_1Al_3(OH)_m/CN_x$ composite showed a superior specific capacitance value along with long term cyclic stability.

Experimental

Materials

Al $(NO_3)_3 \cdot 9H_2O$ (aluminum(III)nitrate nonahydrate) and Co $(NO_3)_2 \cdot 6H_2O$ (cobalt(II)nitrate hexahydrate) were purchased from Merck (India). Hexamethylenetetramine (HMT), NH_2CONH_2

(Urea) and KOH (potassium hydroxide) were obtained from Thermo Fisher scientific India. NH_4F (Ammonium fluoride) was purchased from HI Media India. All the chemicals were used directly without any additional purification. Deionized water (DI H_2O) was obtained from an ultrafiltration system (Milli-Q) at room temperature with a resistivity of 19.0 MΩ cm.

Synthesis of CN_x

Carbon nitride was synthesized from urea using a modified procedure similar to the reported literature.[18,19] 5 g of urea was taken in a porcelain crucible and covered with a Petri dish followed by heating at a temperature of 500 °C for three hours in a muffle furnace. The resulting yellow colored product was washed several times with ethanol to remove any unwanted residues and allowed to dry to obtain the desired product.

Synthesis of $Co_1Al_\delta(OH)_m/CN_x$ composites

In a typical procedure, 35 mg of CN_x was added to a beaker containing 20 mL of DI H_2O and allowed to sonicate for 15 min. Into this, $Co(NO_3)_2 \cdot 6H_2O$ and $Al(NO_3)_3 \cdot 9H_2O$ were added varying in a molar ratio of 1:1, 1:2, 1:3 and 1:4 in order to attain a total molarity of 40 mM. To this above mixture solution, 214 mmol of HMT and 135 mmol of NH_4F were added and stirred to get a homogeneous mixture. Then the mixture solutions were sealed into a 50 mL Stainless steel autoclave reactor and allowed to heat at 120 °C for 6 h. After the heating was completed, the autoclave reactor was allowed to cool naturally to room temperature. Then the obtained precipitates were centrifuged at 1000 rpm and washed with DI H_2O followed by ethanol several times to obtain $Co_1Al_\delta(OH)_m/CN_x$. The $Co_1Al_\delta(OH)_m/CN_x$ was named according to their Co/Al molar ratio. Also only $Co_1Al_3(OH)_m$ was synthesized using a procedure the same as the above except using CN_x.

Electrode fabrication

Fabrication of a working electrode was carried out on a piece of Ni foam with an area of 1 × 1 cm². In order to wipe off the oxide layers, the electrode was washed in 3 M HCl for 30 min and then cleaned with DI H_2O and then ethanol followed by drying. Homogenous slurry was prepared using a polyvinylidene fluoride (PVDF) binder in *N*-methyl-2-pyrrolidone (NMP), conductive carbon (CC) and active materials in 10:10:80 weight percent and coated on the 1 × 1 cm² Ni foam and dried. The weight of the active material on the Ni foam in a single electrode was 1 mg. For designing ASC, active material was used as the cathode, activated carbon (AC) as the anode and cellulose paper as the separator. Before the electrochemical performance the separator was soaked in 2 M KOH. From the calculation, mass loading of positive and negative electrodes were taken to be 1 mg and 5.4 mg and the weight ratio of positive and negative electrodes was found to be 0.185.

Results and discussion

Structural and morphological characterizations

The crystal structure of as synthesized $Co_1Al_\delta(OH)_m/CN_x$ (δ = 1–4), $Al(OH)_x/CN_x$ and $Co(OH)_2/CN_x$ composites were characterized by

using powder X-ray diffraction (p-XRD). Fig. 1(a–c) show the diffraction pattern of $Co_1Al_1(OH)_m/CN_x$, $Co_1Al_2(OH)_m/CN_x$ and $Co_1Al_3(OH)_m/CN_x$ composites respectively. The XRD peaks of $Co_1Al_1(OH)_m/CN_x$ and $Co_1Al_2(OH)_m/CN_x$ composite at $11.74°$, $23.6°$, $34.67°$, $37.39°$, $39.32°$, $46.92°$, $60.37°$, $61.69°$, and $65.7°$ correspond to the (003), (006), (012), (104), (015), (018), (110), (113), and (116) planes of CoAl LDH structure (PDF 04-014-8855) and the peak at $27.3°$ corresponds to the (002) plane of CN_x. The (003) diffraction peak at a 2θ value of $11.74°$ corresponding to the d-spacing of 0.75 nm indicates the presence of CO_3^{2-} ions and H_2O molecules in the interlayer space.[20] As displayed in Fig. 1(c), in the XRD pattern of $Co_1Al_3(OH)_m/CN_x$ along with the peaks of LDH structure, additional peaks of $Al(OH)_x$ were observed. On moving from $Co_1Al_1(OH)_m/CN_x$ to $Co_1Al_3(OH)_m/CN_x$, the left shift of the XRD peak corresponding to the (003) plane is due to the increasing amount of Co/Al ratio.[12,13,21]

The peak corresponding to the (003) plane moves from a 2θ value of $11.74°$ to $9.62°$ and $9.5°$ for $Co_1Al_1(OH)_m/CN_x$, $Co_1Al_2(OH)_m/CN_x$, and $Co_1Al_3(OH)_m/CN_x$ respectively. This indicates that with an increasing amount of Co/Al ratio the interlayer spacing increases.[13] In the case of $Co_1Al_3(OH)_m/CN_x$ the peaks at 2θ values of $15.79°$, $31.56°$, $45.08°$, $48°$ and $52.59°$ correspond to the (111), (222), (422), (511) and (440) plane of $Al(OH)_x$ (PDF-00-060-0273). The XRD pattern of CN_x is shown in Fig. S1 (ESI†) which shows a typical diffraction peak at a 2θ value of $27.3°$ indexed to the plane (002) of graphitic carbon nitride. The p-XRD patterns of only $Al(OH)_x/CN_x$, $Co(OH)_2/CN_x$ and $Co_1Al_3(OH)_m$ are shown in Fig. S2(a, b) and S3 (ESI†) respectively. The average grain size was calculated by using Scherrer's

equation, $D = (k\lambda)/(\beta \cos\theta)$, where D is the grain size, k is the shape factor with a typical value of 0.94, λ is the X-ray wavelength (0.154 nm), β is the full width at half maximum (fwhm), and θ is Bragg's angle. The average crystallite sizes of the $Co_1Al_1(OH)_m/CN_x$, $Co_1Al_2(OH)_m/CN_x$ and $Co_1Al_3(OH)_m/CN_x$, composite materials are found to be 35.05, 24.40 and 15.05 nm respectively. Fig. 1(d) shows the Fourier transform infrared (FTIR) spectra of $Co_1Al_3(OH)_m$ and $Co_1Al_3(OH)_m/CN_x$ composites. A broad peak at around 3485 cm^{-1} in both the samples is due to the structural –OH group stretching vibrations of water molecules. The band at 1630 cm^{-1} is due to the bending vibrations of H_2O and the band at 1360 cm^{-1} indicates the presence of the interlayered CO_3^{2-} ion (C–O vibrations). The absorption bands below a wavelength of 800 cm^{-1} indicates the stretching as well as bending modes of the metal oxygen (M–O) bond in the hydrotalcite structure[22] of LDH.

The specific surface area (SSA) as well as the porosity are considered as crucial aspects for the improvement of electrochemical activities of the supercapacitor electrode materials. The N^2 adsorption–desorption isotherms were used to determine the SSA as well as the average pore size distribution (PSD) of $Co_1Al_3(OH)_m/CN_x$ and $Co_1Al_3(OH)_m$ composites. Fig. 1(e) represents a type IV adsorption/desorption isotherm with an obvious type-H3 hysteresis loop ($P/P_0 > 0.4$) indicating the typical mesoporous nature[17,23] of the $Co_1Al_3(OH)_m/CN_x$ composite. Total BET SSA values of $Co_1Al_3(OH)_m/CN_x$ and $Co_1Al_3(OH)_m$ composites were found to be 72.78 m^2 g^{-1} and 52.051 m^2 g^{-1} which indicates that the SSA for $Co_1Al_3(OH)_m/CN_x$ is much higher than that of $Co_1Al_3(OH)_m$. This high SSA of the $Co_1Al_3(OH)_m/CN_x$ composite is
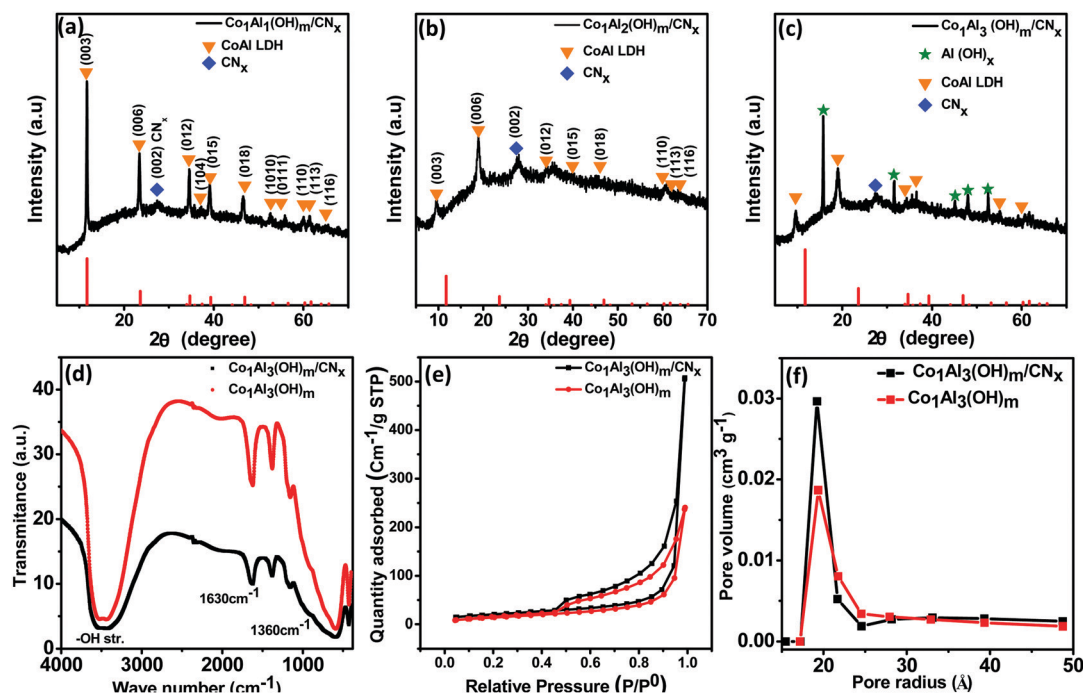
Fig. 1 XRD patterns of (a) $Co_1Al_1(OH)_m/CN_x$, (b) $Co_1Al_2(OH)_m/CN_x$ and (c) $Co_1Al_3(OH)_m/CN_x$. (d) Comparison of the FT-IR for the $Co_1Al_3(OH)_m/CN_x$ composite and $Co_1Al_3(OH)_m$, (e and f) N_2 adsorption–desorption isotherm and BJH pore size distribution of the $Co_1Al_3(OH)_m/CN_x$ composite and only $Co_1Al_3(OH)_m$.

believed to provide a large electrolyte–electrode interface for accumulation of charge electrostatically and the transportation of ions are facilitated by increasing electrical contact as well as by shortening the diffusion path.[17] The average pore radius of the samples are determined from the Barrett–Joyner–Halenda (BJH) pore size distribution analysis and the average pore radius of the composites are lying below 40 Å. The average pore radius of the $Co_1Al_3(OH)_m/CN_x$ and $Co_1Al_3(OH)_m$ composites are found to be 19.36 Å and 19.2 Å respectively which indicates the $Co_1Al_3(OH)_m$ composite has smaller mesopores than the $Co_1Al_3(OH)_m/CN_x$ composite which is shown in Fig. 1(f). From the above obtained results, it can be stated that the introduction of CN_x in the LDH plays a vital role for the improvement of the dispersibility of LDH as well as the formation of the mesopore structure of the $Co_1Al_3(OH)_m/CN_x$ composite[24] which also suggests that the participation of the small amount of CN_x relieves the agglomeration in the LDH layers.[25]

The scanning electron microscopy (SEM) and transmission electron microscopy (TEM) analysis were performed to characterize the morphological features of the $Co_1Al_3(OH)_m/CN_x$ composite at different magnifications. Fig. 2(a and b) show the FESEM images of $Co_1Al_3(OH)_m/CN_x$. The 2D nanosheets were self-assembled to form a 3D nanoflower type structure with a smooth surface to provide sufficient surface area which allows an easy passage of electrolytes through the nanosheets resulting in high capacitive performance.[26] From the EDAX analysis, the presence of all the elements in $Co_1Al_\delta(OH)_m/CN_x$ ($\delta = 1$–4) were confirmed. Fig. S4(a–f) (ESI†) presents the FESEM image and corresponding elemental mappings of C, N, Co, Al and O which clearly shows the uniform distribution of elements over the nanocomposite structure of $Co_1Al_3(OH)_m/CN_x$ and

Fig. S4(g) (ESI†) shows the corresponding EDAX spectra. From elemental mapping, the percentages of elements were calculated and are shown in Fig. S4(h) (ESI†). The atomic percentage of Al and Co were found to be 15.70% and 5.40% respectively with a ratio of 2.9 which is close to the precursor ratio taken during synthesis. The atomic percentage of Co and Al present in all the composites of $Co_1Al_\delta(OH)_m/CN_x$ ($\delta = 1$–4) are shown in Table S1 (ESI†) which is in good accordance with the amount of precursor used during synthesis.

SEM images of CN_x are shown in Fig. S5(a and b) (ESI†) which shows the sheet type morphology of CN_x. Fig. 2(c and d) represent the low-resolution transmission electron microscopy images of the $Co_1Al_3(OH)_m/CN_x$ composite which shows the presence of nanosheets of LDH structure along with some amount of cubic aluminium hydroxides distributed over the sheets. High resolution transmission electron microscopy (HRTEM) images of $Co_1Al_3(OH)_m/CN_x$ are displayed in Fig. 2(e and f) and the lattice fringes with an interplanar distance of 0.56 nm and 0.24 nm were indexed to the (111) and (015) planes of aluminium hydroxide and CoAl LDH structure respectively, which is well consistent with the p-XRD data.

ICP-OES measurement was carried out to determine a more accurate composition of the composite and to calculate the metal ion content of $Co_1Al_3(OH)_m/CN_x$. The $Co_1Al_3(OH)_m/CN_x$ composite contains 23.3% of Al and 7.9% of Co while the Al/Co atomic ratio was obtained to be 2.95 : 1 which is very close to the SEM EDAX analysis data of $Co_1Al_3(OH)_m/CN_x$. In addition to this, the CHN analysis of CN_x and $Co_1Al_3(OH)_m/CN_x$ composite was performed to determine the percentage of nitrogen and carbon present in it. From the CHN analysis the N/C ratio in only CN_x is found to be 1.75 where for the $Co_1Al_3(OH)_m/CN_x$
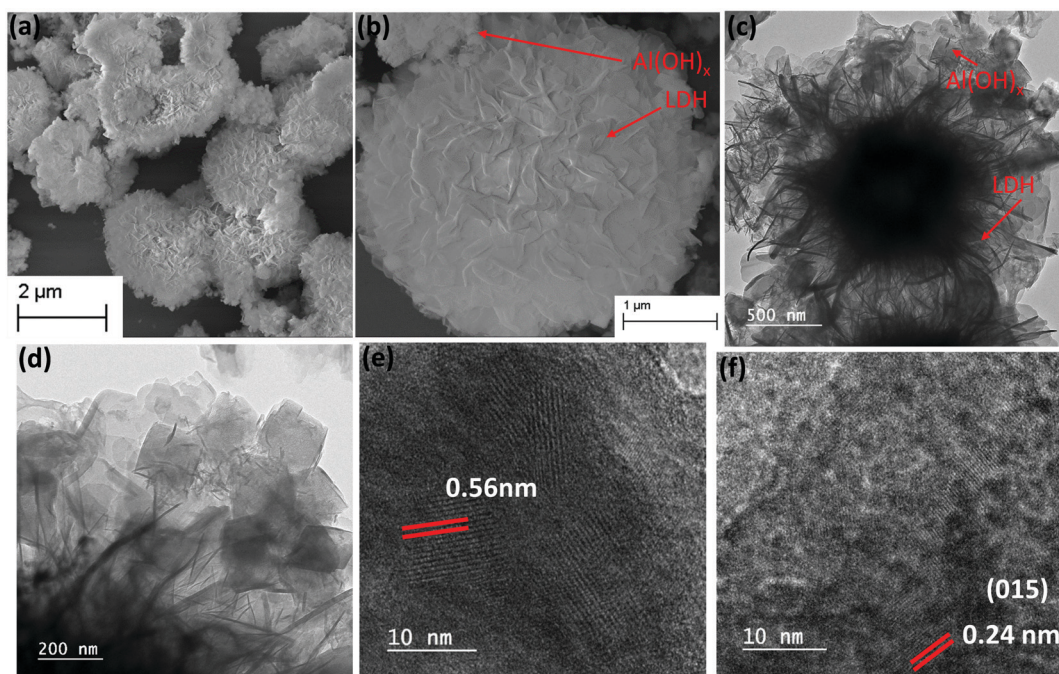

Fig. 2 (a and b) FESEM images, and (c–f) low and high resolution TEM images of $Co_1Al_3(OH)_m/CN_x$.

composite the N/C ratio was 1.68. The ratio of N/C in CN_x was higher than in the $Co_1Al_3(OH)_m/CN_x$ composite which might be because of the loss of nitrogen-containing groups during hydrothermal synthesis.[3]

X-ray photoelectron spectroscopy (XPS) measurements were obtained for better analysis of the surface oxidation state of $Co_1Al_3(OH)_m/CN_x$ composites. XPS studies were carried out using monochromatic Mg Kα as a source. The XPS spectra were charge corrected with respect to the C 1s peak. Fig. 3(a) presents the XPS survey scan of the $Co_1Al_3(OH)_m/CN_x$ composite that confirms the presence of Co, Al, O, N and C elements with binding energies ranging from 0 to 800 eV. The high resolution XPS spectra of Co 2p are shown in Fig. 3(b) which appears in the spectrum as a doublet of $2p_{3/2}$ and $2p_{1/2}$. The $2p_{3/2}$ and $2p_{1/2}$ spectra of Co were decomposed to four peaks. The Co $2p_{3/2}$ peak was deconvoluted into two peaks at 780.48 eV and 782.24 eV corresponding to Co^{2+} and Co^{3+} oxidation states. An additional peak at 789.2 eV is a satellite peak. Similarly Co $2p_{1/2}$ was also deconvoluted into two peaks at 796.03 eV and 797.5 eV due to the presence of the Co^{2+} and Co^{3+} oxidation state. This confirms the coexistence of Co^{2+} and Co^{3+} species. The relative percentage area of Co^{+2} and Co^{+3} and the atomic ratio of Co^{+2}/Co^{+3} for $2p_{3/2}$ and $2p_{1/2}$ are provided in Table S2 (ESI†). The atomic ratio of Co^{+2}/Co^{+3} was obtained by integrating the area of deconvoluted Co^{+2} and Co^{+3} peaks and was found to be nearly 1.95. It has been reported that the presence of Co^{3+} enhances the conductivity of the CoAl LDH structure. Hence the presence of Co^{3+} could be one of the possible factors for better electrochemical behaviour of the electrode material. The high resolution XPS spectra of Al 2p is provided in Fig. 3(c) and a singlet peak centred at 74.28 eV can be ascribed to the Al^{3+} oxidation state. The XPS spectra of

O 1s is given in Fig. 3(d) and it is deconvoluted into three peaks centred at 530.54, 531.9 and 532.72 eV which can be assigned to the metal–hydroxyl bond, adsorbed H_2O and C–O bond respectively. The high resolution 1s XPS peaks of carbon, shown in Fig. 3(e), can be deconvoluted into three peaks. The peak at 284.2 eV is because of the C–C bond whereas the peaks at 285.5 eV and 286.9 eV are because of C–OH bonds and C=C bonds indicating the presence of an CO_3^{2-} intercalated anion in the LDH12. Fig. 3(f) displays the high resolution N 1s XPS spectra which can be deconvoluted into three different peaks. The peak position at 398.3 eV refers to graphitic nitrogen whereas the peaks at 398.9 eV and 402.2 eV are assigned for pyridinic nitrogen and pyrrolic nitrogen respectively.[27,28]

Electrochemical analysis

The electrochemical measurements of $Co_1Al_\delta(OH)_m/CN_x$ ($\delta = 1$–4) and $Co_1Al_3(OH)_m$ composites were investigated in a standard three-electrode system through cyclic voltammetry (CV), galvanostatic charge discharge (GCD) and electrochemical impedance spectroscopy (EIS) measurements at a voltage range of 0–0.55 V in 2 M KOH. The preparation method for the electrodes is briefly explained in the electrode fabrication section. Fig. 4(a) displays the comparison of the CV curve of $Co_1Al_\delta(OH)_m/CN_x$ ($\delta = 1$–4) and only $Co_1Al_3(OH)_m$ at a sweep rate of 30 mV s^{-1}. All the CV curves exhibit similar shapes and for each CV cycle there is a pair of redox peaks which is due to the reversible reaction occurring between Co^{+2} to Co^{+3} and vice-versa present in $Co_1Al_3(OH)_m$ LDH. The CV integral area for the $Co_1Al_3(OH)_m/CN_x$ composite is much larger than other composites. The $Co_1Al_3(OH)_m/CN_x$ composite shows reversible cathodic and anodic peaks at 0.47 and 0.27 V respectively which are shifted from the initial value
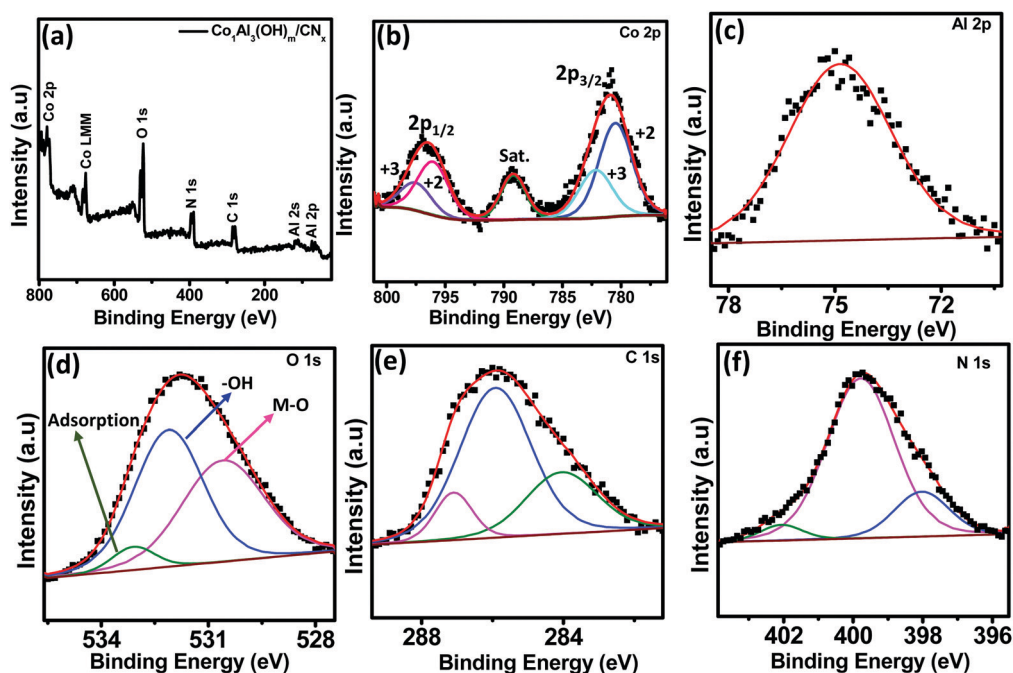

Fig. 3 (a) XPS survey spectrum of the $Co_1Al_3(OH)_m/CN_x$ composite. High resolution XPS spectra of (b) Co 2p, (c) Al 2p, (d) O 1s, (e) C 1s and (f) N 1s respectively.
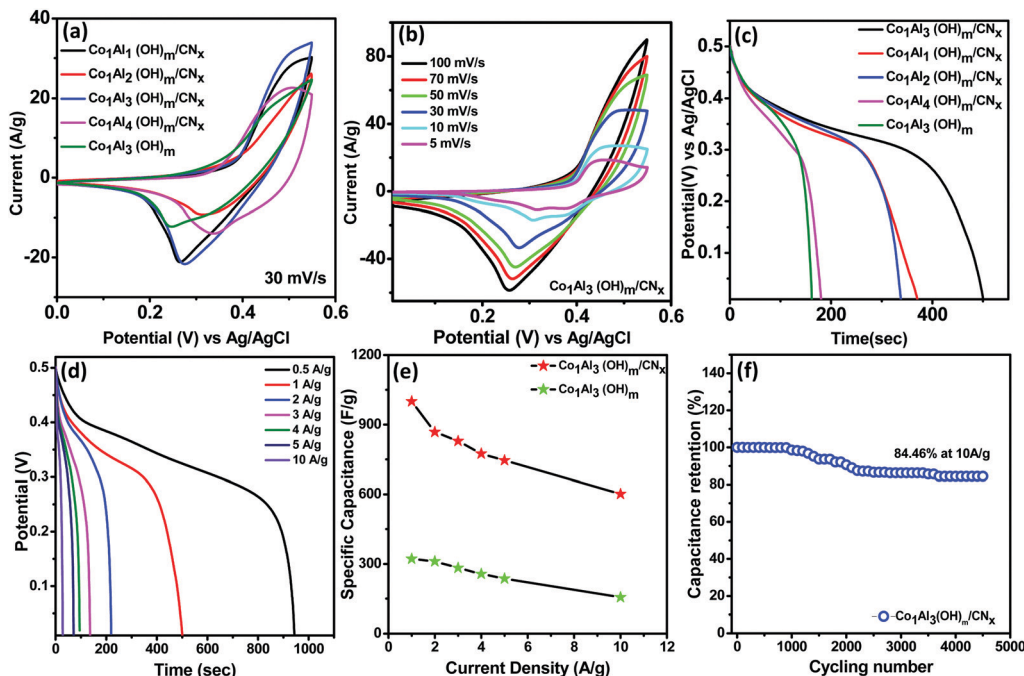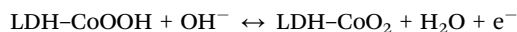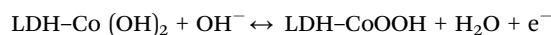
Fig. 4 (a) CV curves of $Co_1Al_\delta(OH)_m/CN_x$ (δ = 1–4) and $Co_1Al_3(OH)_m$ at a scan rate of 30 mV s^{-1}. (b) CV curves of $Co_1Al_3(OH)_m/CN_x$ at different sweep rates (5–100 mV s^{-1}). (c) Comparison of the GCD curves of $Co_1Al_\delta(OH)_m/CN_x$ (δ = 1,2,3,4) with $Co_1Al_3(OH)_m$ at a current density of 1 A g^{-1}. (d) GCD curves of the $Co_1Al_3(OH)_m/CN_x$ composite at current densities of 0.5–10 A g^{-1}. (e) Plot of specific capacitance of $Co_1Al_3(OH)_m/CN_x$ with respect to current density. (f) Plot of percentage capacitance retention (%) with respect to cycling number at a current density of 10 A g^{-1}.

compared to the $Co_1Al_3(OH)_m$ composite. This shift in peak position may be attributed due to the presence of CN_x.[20] The redox peaks for $Co_1Al_3(OH)_m/CN_x$ are because of the faradaic redox reaction occurring between LDH–Co–OH and LDH–Co–O–O–H which can be represented as follows.[13,17,29,30]

$$LDH\text{–}Co\,(OH)_2 + OH^- \leftrightarrow LDH\text{–}CoOOH + H_2O + e^-$$

$$LDH\text{–}CoOOH + OH^- \leftrightarrow LDH\text{–}CoO_2 + H_2O + e^-$$

During the redox reaction, Al^{+3} is non electroactive but this promotes the oxidation of Co^{+2} to Co^{+3} which improves the electrochemical activity of the $Co_1Al_3(OH)_m/CN_x$ composite.[29,31]

Due to the introduction of Al^{+3} in LDH, the crystallinity and hydrophilicity of LDHs are improved which is useful to improve the charge transport and utilization of electrolytes.[29,32,33]

The CV curves of the $Co_1Al_3(OH)_m/CN_x$ composite at different sweep rates from 5 mV s^{-1} to 100 mV s^{-1} in a voltage window varying from 0–0.55 V are displayed in Fig. 4(b). With increase in scan rate, the potential difference between the cathodic and anodic peak increases[34,35] and the current also increases gradually with an increase in sweep rate indicating the good electrochemical responses of the $Co_1Al_3(OH)_m/CN_x$ composite.[36] The area under the CV curve at different sweep rates for $Co_1Al_3(OH)_m/CN_x$ is much larger than that for only $Co_1Al_3(OH)_m$ which indicates that $Co_1Al_3(OH)_m/CN_x$ shows a higher specific capacitance.[34] The specific capacitance value for the $Co_1Al_3(OH)_m/CN_x$ composite was found to be 821.81 F g^{-1} and 594.73 F g^{-1} at a sweep rate of 5 mV s^{-1} and 10 mV s^{-1}

respectively and for $Co_1Al_3(OH)_3$ it was found to be 611.87 F g^{-1} and 549.09 F g^{-1} which are calculated from the area under the CV curve. The presence of CN_x promotes the SSA as well as conductivity of the $Co_1Al_3(OH)_m/CN_x$ composite enhancing the electrochemical behaviour of the material. High SSA is one of the important factors for increased faradaic reaction between the electrolyte and electrode material and the increase in conductivity promotes the transfer of electrons in the redox reaction. Moreover the synergic interaction between LDH and CN_x promotes the electrochemical performance[25] of the $Co_1Al_3(OH)_m/CN_x$ composite. Table S3 (ESI†) presents the comparison of the electrochemical performance of the $Co_1Al_3(OH)_m/CN_x$ composite with previously reported literature. Fig. 4(c) presents the comparison of the non-linear GCD curves of $Co_1Al_\delta(OH)_m/CN_x$ (δ = 1–4) and only $Co_1Al_3(OH)_m$ in the potential window of 0–0.5 V at 1 A g^{-1} current density. In order to show the electrochemical contribution of bare Ni foam, GCD measurements were carried out which shows a negligible contribution towards the electrochemical performance as shown in Fig. S6 (ESI†). From the discharge curve, the specific capacitance of $Co_1Al_\delta(OH)_m/CN_x$ (δ = 1–4) composites and $Co_1Al_3(OH)_m$ were calculated to be 102.8 mA h g^{-1} (739 F g^{-1}), 93.7 mA h g^{-1} (674.18 F g^{-1}), 138 mA h g^{-1} (1000 F g^{-1}), and 50 mA h g^{-1} (321 F g^{-1}) respectively under a 1 A g^{-1} current density which implies the specific capacitance of the hybrid materials are enhanced compared to other control samples and also pure $Co_1Al_3(OH)_m$. The non-linear GCD profiles of the composite obtained at 1 to 10 A g^{-1} demonstrate the faradaic behaviour of the electrodes.[22,26] Fig. 4(d) shows the GCD curve of the $Co_1Al_3(OH)_m/CN_x$ composite at a current density ranging

from 0.5 to 10 A g^{-1} and the corresponding specific capacitance was calculated to be 138 mA h g^{-1} (1000 F g^{-1}), 122 mA h g^{-1} (884 F g^{-1}), 96 mA h g^{-1} (690.66 F g^{-1}) and 78 mA h g^{-1} (560 F g^{-1}) under 1, 2, 5 and 10 A g^{-1} current densities respectively. The specific capacitance value increases with a decrease in current density as the diffusion of electrolyte ions gain access to the maximum electrode surface area at a low current density resulting in a high specific capacitance. In the case of higher current density, the decrease in capacitance is due to the reduction in effective interaction between the electrolyte ions and electrode.[25] The composite $Co_1Al_3(OH)_m/CN_x$ retains 69% of its initial specific capacitance at a current density of 5 A g^{-1}.

Fig. 4(e) shows the specific capacitance (F g^{-1}) plot as a function of current densities (A g^{-1}) for $Co_1Al_3(OH)_m/CN_x$ and $Co_1Al_3(OH)_m$ composites. The specific capacitance of only $Co_1Al_3(OH)_m$ is lower than that of $Co_1Al_3(OH)_m/CN_x$ and the high specific capacitance of $Co_1Al_3(OH)_m/CN_x$ correlates with the CV results, high SSA and average pore size distribution results. Fig. 4(f) represents the cyclic durability of the single electrode which shows an excellent 84.46% capacitance retention of thte initial value after 4500 cycles at a current density of 10 A g^{-1}.

In order to give a better explanation for the charge storage mechanism of the electrode material, differentiation of capacitive contribution and diffusive contribution to the total capacitance is important. Capacitive current arises from the electrical double layer (surface ion adsorption/desorption process) which is directly proportional to the sweep rate while diffusion-controlled current arises from the diffusion of electrolyte ions from and into the electrode.[37] At a fixed potential (V), the current (i) can be calculated by using the following eqn (1)[11,38–40]

$$i(V) = k_1\nu + k_2\nu^{1/2} \tag{1}$$

where $k_1\nu$ and $k_2\nu^{1/2}$ represent the capacitive current and diffusion controlled current respectively, k_1 and k_2 are constant and ν is the scan rate. The slope (k_1) can be obtained by plotting i against $\nu^{1/2}$. Fig. 5(a) presents the fractional area of the capacitive contribution of $Co_1Al_3(OH)_m/CN_x$ at a sweep rate of

10 mV s^{-1}. The capacitive contribution for the $Co_1Al_3(OH)_m/CN_x$ sample was calculated to be 5.47 at 5 mV s^{-1} and it increases to 7.56 at a scan rate of 10 mV s^{-1} as shown in Fig. 5(b).

EIS measurements were performed under open circuit potential in the frequency window of 100 kHz to 0.1 Hz for better evaluation of the electrochemical performance of the $Co_1Al_3(OH)_m/CN_x$ composite. The Nyquist plot for $Co_1Al_3(OH)_m/CN_x$ and $Co_1Al_3(OH)_m$ are shown in Fig. 5(c). The $Co_1Al_3(OH)_m/CN_x$ composite shows a lower equivalent series resistance (R_s) value of 0.64 Ω and also a lower charge transfer resistance value than $Co_1Al_3(OH)_m$ (R_s = 0.67 Ω). The more vertical nature of the EIS plot of $Co_1Al_3(OH)_m/CN_x$ than only $Co_1Al_3(OH)_m$ in the low frequency region signifies that the $Co_1Al_3(OH)_m/CN_x$ composite has a high electrochemical capacitive performance compared with $Co_1Al_3(OH)_m$.

Before assembling the asymmetric supercapacitor (ASC), the capacitive performance of activated carbon (AC) was evaluated as AC was used as the negative electrode in the device. Fig. 6(a) represents the CV curves of AC at different sweep rates while GCD curves at different current densities under a voltage range of 0 to −1 V are provided in Fig. 6(b). The rectangular shape of the CV curves having no redox peaks and the symmetrical GCD curves indicate the EDLC type behaviour of AC17. From the CV curves, the specific capacitance values for AC were found to be 260 F g^{-1} and 220 F g^{-1} at sweep rates of 10 and 100 mV s^{-1} respectively while from the GCD curve, it was found to be 135 F g^{-1} at a current density of 1 A g^{-1}.

For the practical application of the $Co_1Al_3(OH)_m/CN_x$ composite, an asymmetric supercapacitor (ASC) device was assembled with $Co_1Al_3(OH)_m/CN_x$ and AC as the cathode and anode respectively. All the electrochemical measurements of the ASC device were performed in 2 M KOH. Fig. 7(a) shows the CV curves of both AC and $Co_1Al_3(OH)_m/CN_x$ at a scan rate of 10 mV s^{-1}. Fig. 7 (b) shows the CV curves of the ASC device measured by varying the potential range from 1 V to 1.8 V. With an increase in potential from 1 V to 1.6 V, the nature of the CV curve does not change, which indicates that the ASC device can work steadily in the potential range of 1.6 V. Fig. 7(c) shows the CV curves in the voltage window of 0–1.6 V for the ASC device at
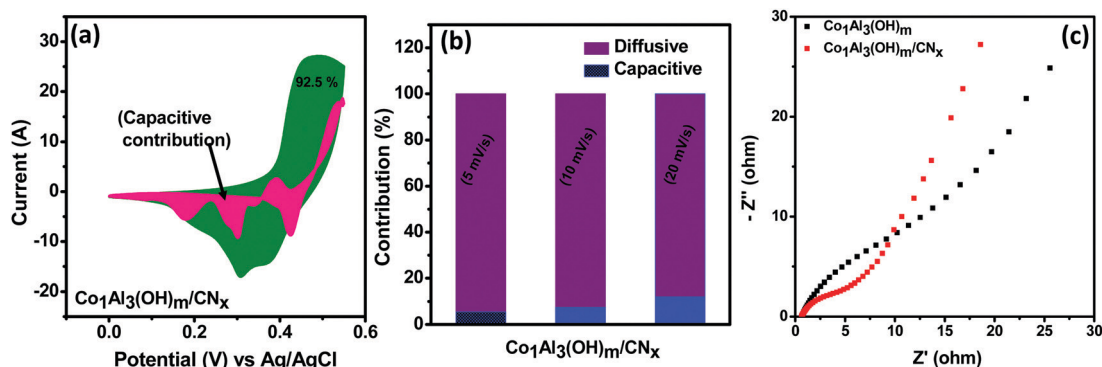

Fig. 5 (a) CV curves of $Co_1Al_3(OH)_m/CN_x$ distinguishing both capacitive and diffusive contribution at a sweep rate of 10 mV s^{-1}. (b) Plot of percentage of capacitive and diffusion-controlled contribution for $Co_1Al_3(OH)_m/CN_x$ at various sweep rates. (c) Nyquist plot of $Co_1Al_3(OH)_m/CN_x$ and $Co_1Al_3(OH)_m$.
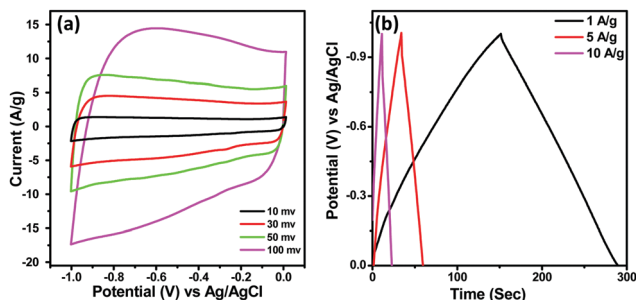
Fig. 6 (a) CV curves of AC at different sweep rates and (b) GCD plot of AC at different current densities.

different sweep rates.[1] At different sweep rates, the nature of the CV curves are similar which indicates the good rate capability of the device.

Fig. 7(d) represents the galvanostatic charge discharge curves at current densities ranging from 1 to 5 A g^{-1} current density. The specific capacitance value for the ASC device was found to be 71.5, 67.13, 43.84, 36.37 and 29.47 F g^{-1} at 1,2,3,4 and 5 A g^{-1} current density respectively which indicates the ~41.21% retention of the initial specific capacitance at a current density of 5 A g^{-1}. The specific capacitance vs current density for Co$_1$Al$_3$(OH)$_m$/CN$_x$//AC ASC is plotted in Fig. 7(e). As the energy density and power density are important parameters for supercapacitors, their evaluation is very much important. Fig. 7(f) represents the Ragone plot for Co$_1$Al$_3$(OH)$_m$/CN$_x$//AC which shows the variation of energy density with change in power density. An energy density value of 22.35 W h kg^{-1} was at a power density of 750.2 W kg^{-1} while the power density was found to be 3613.36 W kg^{-1} at an energy density of 12.89 W h kg^{-1} which is

much higher than the LDH or Co-based ASC devices reported in the literature such as Ni$_x$Co$_{1-x}$ LDH–ZTO//AC (23.7 W h kg^{-1}, 284.2 W kg^{-1}),[41] NiCo$_2$O$_4$–rGO//AC (23.32 W h kg^{-1}, 324.9),[42] NiCo$_2$O$_4$/MnO$_2$//AG (9.4 W h kg^{-1}, 175 W kg^{-1}),[43] Co–Fe LDHs-CFC//AC (16.1 W h kg^{-1}, 399 W kg^{-1}),[44] and C–MnO$_2$12 h (14 W h kg^{-1}, 200 W kg^{-1}).[45] The cycling stability of the Co$_1$Al$_3$(OH)$_m$/CN$_x$//AC ASC device was performed at a current density of 10 A g^{-1} for 8000 cycles and the capacitance retention was found to be 80% which is shown in Fig. 7(g). EIS spectra were measured in the frequency range of 0.1 Hz to 100 kHz and Fig. 7(h) presents the EIS plot of Co$_1$Al$_3$(OH)$_m$/CN$_x$//AC ASC along with the equivalent circuit. R_s, R_{ct}, CPE and W represent the equivalent series resistance, charge transfer resistance, constant phase element and Warburg impedance respectively. The R_s for ASC was obtained to be 0.89 Ω and the R_{ct} value was found to be 1.18 Ω which was calculated by fitting the experimental data with an equivalent circuit. The low value of R_{ct} signifies the low resistance and high charge transfer property of the material.

The high capacitance of the Co$_1$Al$_3$(OH)$_m$/CN$_x$ composite can be attributed to the following factors:

(i) The presence of CN$_x$ in the Co$_1$Al$_3$(OH)$_m$ LDH composite improves the dispensability of the LDH and hence improves the charge transfer property of the material which in turn improves the electrochemical performance.[1,46–49] It prevents the rapid agglomeration of layered materials and hence provides high structural and chemical stability during the electrochemical process.[1,46,48]

(ii) The introduction of Al in the LDH increases the formation of more Co^{3+} ions in the interlayer of the LDH composite which enhances the conductivity and electrochemical performance of the material.[29–31,33]
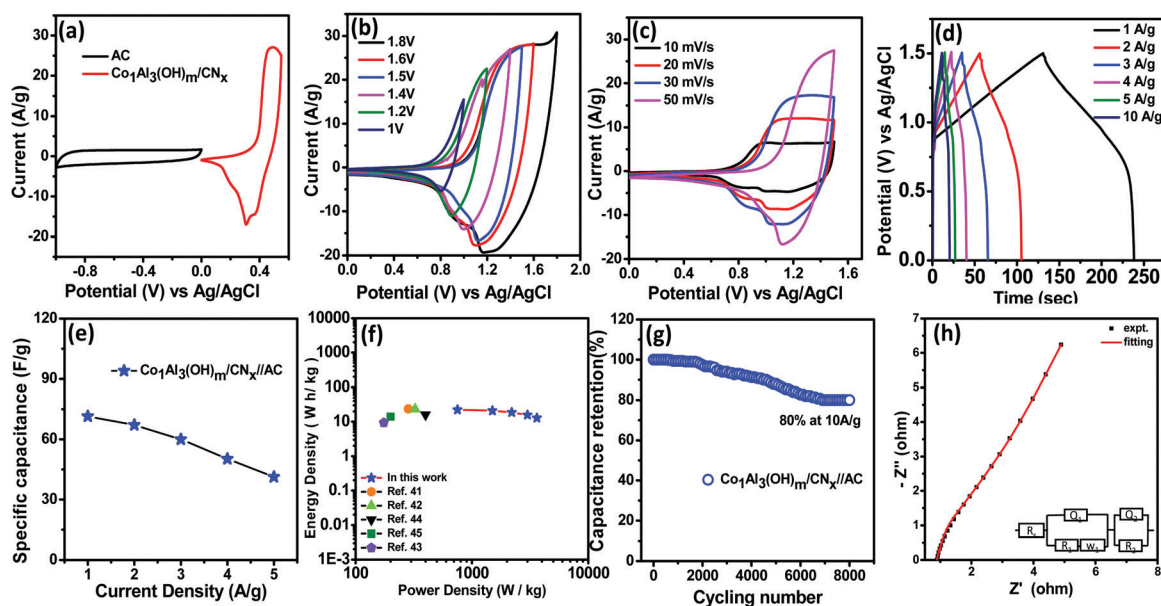

Fig. 7 Electrochemical behavior of ASC Co$_1$Al$_3$(OH)$_m$/CN$_x$//AC. (a) CV curves of AC and Co$_1$Al$_3$(OH)$_m$/CN$_x$ at a sweep rate of 10 mV s^{-1}. (b) CV curves of ASC at different potential ranges. (c) CV curves of ASC at different sweep rates. (d) GCD curves at different current densities. (e) Specific capacitance at different current densities. (f) Ragone plot of the Co$_1$Al$_3$(OH)$_m$/CN$_x$//AC asymmetric supercapacitor. (g) Cyclic stability of the ASC at a current density of 10 A g^{-1}. (h) EIS curve of the ASC.

(iii) The synergetic interaction of the CN_x and $Co_1Al_3(OH)_m$ LDH is another possible factor for increased electrochemical performances of the $Co_1Al_3(OH)_m/CN_x$ electrode material where CN_x provides a large active surface area for effective transfer of electrons and restricts the stacking of the LDH.[25] Hence the interfacial contact can be enhanced by anchoring CN_x on the layered material resulting in fast and smooth ion diffusion through the layered structure.

(iv) The high SSA of the $Co_1Al_3(OH)_m/CN_x$ composite compared to $Co_1Al_3(OH)_m$ provides a large interface between electrolyte–electrode for electrostatic charge accumulation and it facilitates the transport of ions by increasing the electrical contact as well as by shortening the diffusion path.[17]

Conclusions

In this work we have synthesised $Co_1Al_3(OH)_m/CN_x$ composites by one-pot hydrothermal synthesis method for supercapacitor applications. The as-synthesised composite shows a 3D nano-flower type structure with a smooth surface which is believed to improve the electrochemical performance of the composite. The maximum specific capacitance for $Co_1Al_3(OH)_m/CN_x$ was obtained to be 138 mA h g^{-1} (1000 F g^{-1}) at a current density of 1 A g^{-1} (approximately 3 times higher than that of $Co_1Al_3(OH)_m$) and capacitance retention of 84.46% even after 4500 cycles. Furthermore the ASC provides an energy density of 22.35 W h kg^{-1} at a power density of 750.2 W kg^{-1} with 80% capacitive retention even after 8000 cycles at a current density of 10 A g^{-1}. The synergetic interaction between CN_x and $Co_1Al_3(OH)_m$ LDH provides a large electroactive surface providing faster ion diffusion through the LDH structure. Moreover the $Co_1Al_3(OH)_m/CN_x$ composite with a superior capacitance along with long term stability makes it a promising electrode material for supercapacitor applications.

Conflicts of interest

There are no conflicts to declare.

Acknowledgements

References

1 C. Jing, B. Dong and Y. Zhang, *Energy Environ. Mater.*, 2020, **3**, 346–379.

2 X. Li, D. Du, Y. Zhang, W. Xing, Q. Xue and Z. Yan, *J. Mater. Chem. A*, 2017, **5**, 15460–15485.

3 T. Bhowmik, R. Mishra and S. Barman, *Energy Fuels*, 2021, **35**, 5206–5216.

4 N. L. Wulan Septiani, Y. V. Kaneti, K. B. Fathoni, J. Wang, Y. Ide, B. Yuliarto, Nugraha, H. K. Dipojono, A. K. Nanjundan, D. Golberg, Y. Bando and Y. Yamauchi, *Nano Energy*, 2020, **67**, 104270.

5 K.-B. Wang, Q. Xun and Q. Zhang, *EnergyChem*, 2020, **2**, 100025.

6 Y. Li, J. Henzie, T. Park, J. Wang, C. Young, H. Xie, J. W. Yi, J. Li, M. Kim, J. Kim, Y. Yamauchi and J. Na, *Bull. Chem. Soc. Jpn.*, 2019, **93**, 176–181.

7 K.-B. Wang, R. Bi, Z.-K. Wang, Y. Chu and H. Wu, *New J. Chem.*, 2020, **44**, 3147–3167.

8 J. Tang, R. R. Salunkhe, H. Zhang, V. Malgras, T. Ahamad, S. M. Alshehri, N. Kobayashi, S. Tominaka, Y. Ide, J. H. Kim and Y. Yamauchi, *Sci. Rep.*, 2016, **6**, 30295.

9 R. Mishra, P. Panda and S. Barman, *New J. Chem.*, 2021, **45**, 5897–5906.

10 J.-H. Cha, E. B. Park, S. W. Han, Y. D. Kim and D.-Y. Jung, *Chem. – Asian J.*, 2019, **14**, 446–453.

11 C. Li, Y. Zhou, X. Li, H. Wang, P. Huo and X. Wang, *Appl. Surf. Sci.*, 2021, **536**, 147780.

12 G. Wang and Z. Jin, *J. Mater. Chem. C*, 2021, **9**, 620–632.

13 G. Li, X. Zhang, D. Qiu, Z. Liu, C. Yang, C. B. Cockreham, B. Wang, L. Fu, J. Zhang, B. Sudduth, X. Guo, H. Sun, Z. Huang, J. Qi, J. Sun, S. Ha, Y. Wang and D. Wu, *Adv. Electron. Mater.*, 2019, **5**, 1900215.

14 T. Wang, S. Zhang, X. Yan, M. Lyu, L. Wang, J. Bell and H. Wang, *ACS Appl. Mater. Interfaces*, 2017, **9**, 15510–15524.

15 X. Xu, J. Tang, H. Qian, S. Hou, Y. Bando, M. S. A. Hossain, L. Pan and Y. Yamauchi, *ACS Appl. Mater. Interfaces*, 2017, **9**, 38737–38744.

16 H. Tian, W. Bao, Y. Jiang, L. Wang, L. Zhang, O. Sha, C. Wu and F. Gao, *Chem. Eng. J.*, 2018, **354**, 1132–1140.

17 S. Sanati and Z. Rezvani, *Chem. Eng. J.*, 2019, **362**, 743–757.

18 Y. Zheng, Z. Zhang and C. Li, *J. Photochem. Photobiol., A*, 2017, **332**, 32–44.

19 Y. Zhang, J. Liu, G. Wu and W. Chen, *Nanoscale*, 2012, **4**, 5300–5303.

20 T. M. Masikhwa, M. J. Madito, D. Y. Momodu, J. K. Dangbegnon, O. Guellati, A. Harat, M. Guerioune, F. Barzegar and N. Manyala, *RSC Adv.*, 2016, **6**, 46723–46732.

21 H. Wang, X. Xiang and F. Li, *J. Mater. Chem.*, 2010, **20**, 3944–3952.

22 J. Fang, M. Li, Q. Li, W. Zhang, Q. Shou, F. Liu, X. Zhang and J. Cheng, *Electrochim. Acta*, 2012, **85**, 248–255.

23 W. Yang, Z. Gao, J. Wang, J. Ma, M. Zhang and L. Liu, *ACS Appl. Mater. Interfaces*, 2013, **5**, 5443–5454.

24 L. Zhang, M. Ou, H. Yao, Z. Li, D. Qu, F. Liu, J. Wang, J. Wang and Z. Li, *Electrochim. Acta*, 2015, **186**, 292–301.

25 B. Patil, C. Park and H. Ahn, *RSC Adv.*, 2019, **9**, 33643–33652.

26 T. Li, G. H. Li, L. H. Li, L. Liu, Y. Xu, H. Y. Ding and T. Zhang, *ACS Appl. Mater. Interfaces*, 2016, **8**, 2562–2572.

27 M. Arif, G. Yasin, M. Shakeel, M. A. Mushtaq, W. Ye, X. Fang, S. Ji and D. Yan, *Mater. Chem. Front.*, 2019, **3**, 520–531.

28 M. Arif, G. Yasin, M. Shakeel, X. Fang, R. Gao, S. Ji and D. Yan, *Chem. – Asian J.*, 2018, **13**, 1045–1052.

29 J. Li, P. Zhang, X. Zhao, L. Chen, J. Shen, M. Li, B. Ji, L. Song, Y. Wu and D. Liu, *J. Colloid Interface Sci.*, 2019, **549**, 236–245.

30 E. Scavetta, B. Ballarin, M. Gazzano and D. Tonelli, *Electrochim. Acta*, 2009, **54**, 1027–1033.

31 Q. Zhang, B. Zhao, J. Wang, C. Qu, H. Sun, K. Zhang and M. Liu, *Nano Energy*, 2016, **28**, 475–485.

32 X. Wang, Y. Lin, Y. Su, B. Zhang, C. Li, H. Wang and L. Wang, *Electrochim. Acta*, 2017, **225**, 263–271.

33 L. Qian, Z. Lu, T. Xu, X. Wu, Y. Tian, Y. Li, Z. Huo, X. Sun and X. Duan, *Adv. Energy Mater.*, 2015, **5**, 1500245.

34 A. Zhang, C. Wang, Q. Xu, H. Liu, Y. Wang and Y. Xia, *RSC Adv.*, 2015, **5**, 26017–26026.

35 I. Shakir, M. Shahid, U. A. Rana, I. M. A. Nashef and R. Hussain, *Electrochim. Acta*, 2014, **129**, 28–32.

36 C. Jing, Y. Huang, L. Xia, Y. Chen, X. Wang, X. Liu, B. Dong, F. Dong, S. Li and Y. Zhang, *Appl. Surf. Sci.*, 2019, **496**, 143700.

37 K. Wang, R. Bi, M. Huang, B. Lv, H. Wang, C. Li and H. Wu, *Inorg. Chem.*, 2020, **59**, 6808–6814.

38 Q. Yang, Y. Liu, L. Xiao, M. Yan, H. Bai, F. Zhu, Y. Lei and W. Shi, *Chem. Eng. J.*, 2018, **354**, 716–726.

39 K. Wang, Q. Li, Z. Ren, C. Li, Y. Chu, Z. Wang, M. Zhang, H. Wu and Q. Zhang, *Small*, 2020, **16**, 2001987.

40 K. Wang, S. Wang, J. Liu, Y. Guo, F. Mao, H. Wu and Q. Zhang, *ACS Appl. Mater. Interfaces*, 2021, **13**, 15315–15323.

41 X. Wang, A. Sumboja, M. Lin, J. Yan and P. S. Lee, *Nanoscale*, 2012, **4**, 7266–7272.

42 X. Wang, W. S. Liu, X. Lu and P. S. Lee, *J. Mater. Chem.*, 2012, **22**, 23114–23119.

43 M. Kuang, Z. Q. Wen, X. L. Guo, S. M. Zhang and Y. X. Zhang, *J. Power Sources*, 2014, **270**, 426–433.

44 K. Ma, J. P. Cheng, F. Liu and X. Zhang, *J. Alloys Compd.*, 2016, **679**, 277–284.

45 V. J. Mane, D. B. Malavekar, S. B. Ubale, V. C. Lokhande and C. D. Lokhande, *Inorg. Chem. Commun.*, 2020, **115**, 107853.

46 J. Wu, Q. e. Zhang, J. Wang, X. Huang and H. Bai, *Energy Environ. Sci.*, 2018, **11**, 1280–1286.

47 S. Mondal, U. Rana and S. Malik, *Chem. Commun.*, 2015, **51**, 12365–12368.

48 M. Ghaemmaghami and R. Mohammadi, *Sustainable Energy Fuels*, 2019, **3**, 2176–2204.

49 Y. Luo, Y. Yan, S. Zheng, H. Xue and H. Pang, *J. Mater. Chem. A*, 2019, **7**, 901–924.